

# Heterogeneous Nanostructures Fabricated via Binding Energy-Controlled Nanowelding

Zhi-Jun Zhao,<sup>†</sup> Min Gao,<sup>‡</sup> SoonHyoung Hwang,<sup>†</sup> Sohee Jeon,<sup>†</sup> Inkyu Park,<sup>‡</sup> Sang-Hu Park,<sup>§</sup> and Jun-Ho Jeong<sup>\*,†</sup>

<sup>†</sup>Department of Nano Manufacturing Technology, Korea Institute of Machinery and Materials, 156, Gajeongbuk-ro, Yuseong-gu, Daejeon 34113, South Korea

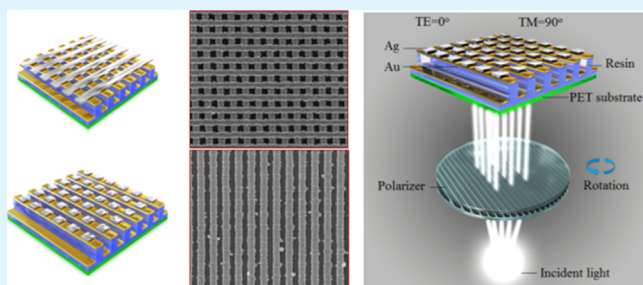
<sup>‡</sup>Department of Mechanical Engineering, Korea Advanced Institute of Technology, Deajeon 34141, Korea

<sup>§</sup>School of Mechanical Engineering, Pusan National University, Busandaehak-ro 63 beon-gil, Geumjeong-gu, Busan 609-735, Republic of Korea

## Supporting Information

**ABSTRACT:** A novel concept for fabricating heterogeneous nanostructures based on different melting temperatures is developed. Au–Ag composite cross-structures are fabricated by nanowelding technologies. During the fabrication of Au–Ag composite cross-structures, Ag nanowires transform into ordered particles decorating the Au nanowire surfaces with an increase in the welding temperature because of the different melting temperatures of Au and Ag. To compare and explain the melting temperatures, the thicknesses of Au and Ag nanowires as parameters are analyzed. Scanning electron microscopy and focused ion beam imaging are used to observe the morphologies and cross sections of the fabricated samples. The evolution of 3D nanostructures is observed by atomic force microscopy, whereas the compositions and binding energies of the nanostructures are determined by X-ray diffraction and X-ray photoelectron spectroscopies. In addition, the atomic structures are analyzed by transmission electron microscopy, and the optical properties of the fabricated nanostructures are evaluated by spectrometry. Furthermore, color filter electrodes are fabricated, and their polarization properties are evaluated by sheet resistance measurements and observing the color and brightness of light-emitting diodes. The proposed method is suitable for application in various fields such as biosensors, optics, and medicine.

**KEYWORDS:** heterogeneous nanostructures, structure–property relationships, metal nanostructures, electro-optical materials, polarization color filter electrode



## 1. INTRODUCTION

With the development of nanotechnology, nanostructures have entered the fields of optics,<sup>1–3</sup> biology,<sup>4,5</sup> medicine,<sup>6–8</sup> and aerospace<sup>9,10</sup> for a wide range of applications. Nanostructures can be fabricated via traditional methods including photolithography,<sup>11,12</sup> electron-beam (e-beam) lithography,<sup>13–15</sup> reactive ion etching,<sup>16,17</sup> inductively coupled plasma,<sup>18,19</sup> nanoimprint lithography,<sup>20,21</sup> deposition,<sup>22,23</sup> microcontact printing,<sup>24</sup> and chemical synthesis.<sup>25,26</sup> With the expansion of nanoscience exploration, the demand for special nanostructures applicable to corresponding fields has increased, and traditional fabrication methods can no longer meet the current application needs. Recently, plasmonic nanostructures with varying designs including holes,<sup>27,28</sup> nanogratings,<sup>29,30</sup> dots,<sup>31,32</sup> cavity-apertures,<sup>33,34</sup> nanorods,<sup>35,36</sup> nanoantennas,<sup>37</sup> biomimetic structural colors,<sup>38,39</sup> 2D Bravais lattices,<sup>40</sup> and nanopath arrays<sup>41</sup> have been widely applied in color filters, digital displays, color printing, sensing, digital imaging, and liquid crystal displays. These nanostructures are generally

fabricated via e-beam lithography, reactive ion etching, deposition, and inductively coupled plasma deposition; however, these technologies have limitations in mass production, large-area synthesis, substrate materials, and economic feasibility.

Nanostructures synthesized by chemicals including the most common Ag and Au nanowires and nanoparticles have been applied in transparent electrodes,<sup>42–45</sup> touch screens,<sup>46,47</sup> and sensors.<sup>48</sup> On the other hand, some composite nanostructures fabricated via e-beam lithography, evaporation, chemical synthesis, and special nanotransfer techniques have been applied in photocatalysis,<sup>49</sup> solar cells,<sup>50</sup> and energy harvesting.<sup>51</sup> The fabrication of these complex composite nanostructures is challenging, which impedes their improvements in applicability and efficacy. Thus, researchers are increasingly

**Received:** October 22, 2018

**Accepted:** January 23, 2019

**Published:** January 23, 2019

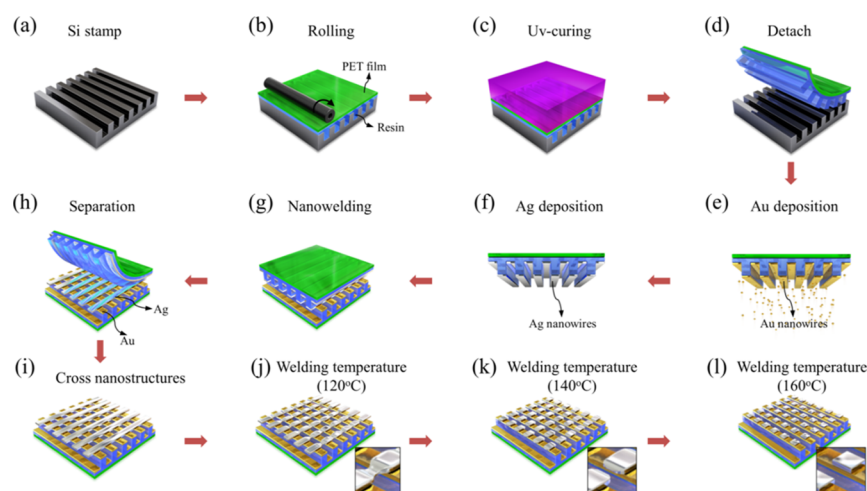


**Figure 1.** Fabrication process of heterogeneous nanostructures via nanowelding. (a) Si stamp, (b) fabrication of polymer mold, (c) UV curing, (d) detachment process, (e,f) deposition of Au and Ag nanowires using e-beam evaporator, (g) nanowelding at a pressure of 600 kPa and 80 °C for 10 min, and (h) separation of mold from the nanostructure. (i–l) Processing of fabricated samples at different melting temperatures (120, 140, and 160 °C).

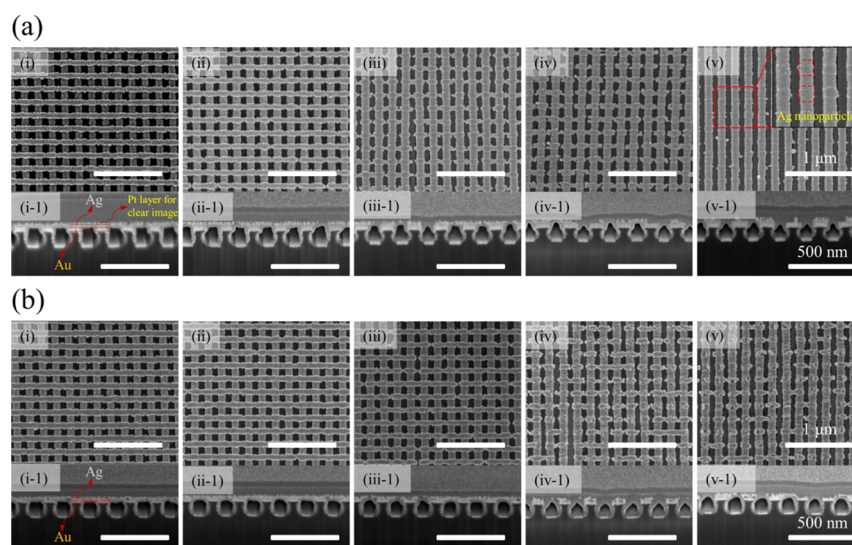


**Figure 2.** SEM and FIB images showing morphologies and cross sections of heterogeneous nanostructures fabricated using Au and Ag nanowires at different temperatures (80–160 °C in steps of 20 °C). (a) Au and Ag nanowires (30 nm thick). (i) Cross nanostructures fabricated at welding temperatures of (i) 80, (ii) 100, (iii) 120, (iv) 140, and (v) 160 °C; (i.1–v.1) cross-sectional images. (b) Au nanowires (10 nm thick) and Ag nanowires (30 nm thick). Cross nanostructures fabricated at (i) 80, (ii) 100, (iii) 120, (iv) 140, and (v) 160 °C; (i.1–v.1) cross-sectional images.

focused on developing complex composite nanostructures to better meet the requirements of specific applications.<sup>52–54</sup> However, the problems of cost and mass production remain to be solved in the fabrication of nanostructures. Our group proposed a fabrication method for cross and composite nanostructures based on nanoimprinting, deposition, and nanowelding. The fabricated cross and composite nanostructures have been applied in polarizing color filters<sup>55–57</sup> and photocatalysis,<sup>58</sup> respectively.

On the basis of our previous research, in this work, we developed a novel nanofabrication method for heterogeneous nanostructures that utilizes different melting temperatures of two metals at the nanoscale. Au and Ag nanowires were fabricated via nanoimprinting and e-beam evaporation. By adjusting the welding temperatures, Ag nanowires could be converted into nanoparticles orderly assembled on the surfaces of the Au nanowires. The morphologies and cross sections

were analyzed by scanning electron microscopy (SEM), atomic force microscopy (AFM), and focused ion beam (FIB) imaging. The atomic structures were observed via transmission electron microscopy (TEM), and the compositions and binding energies of the nanostructures were measured via X-ray diffraction (XRD) analysis and X-ray photoelectron spectroscopy (XPS). Further, the transmissions of the fabricated composite nanostructures were evaluated. In addition, color filter electrodes prepared using the nanostructures were evaluated by measuring their sheet resistances and polarization properties. The proposed method may provide important insights into nanofabrication and the application of complex composite nanostructures.

## 2. RESULTS AND DISCUSSION

### 2.1. Morphologies of Heterogeneous Nanostructures.

Heterogeneous nanostructures were fabricated by

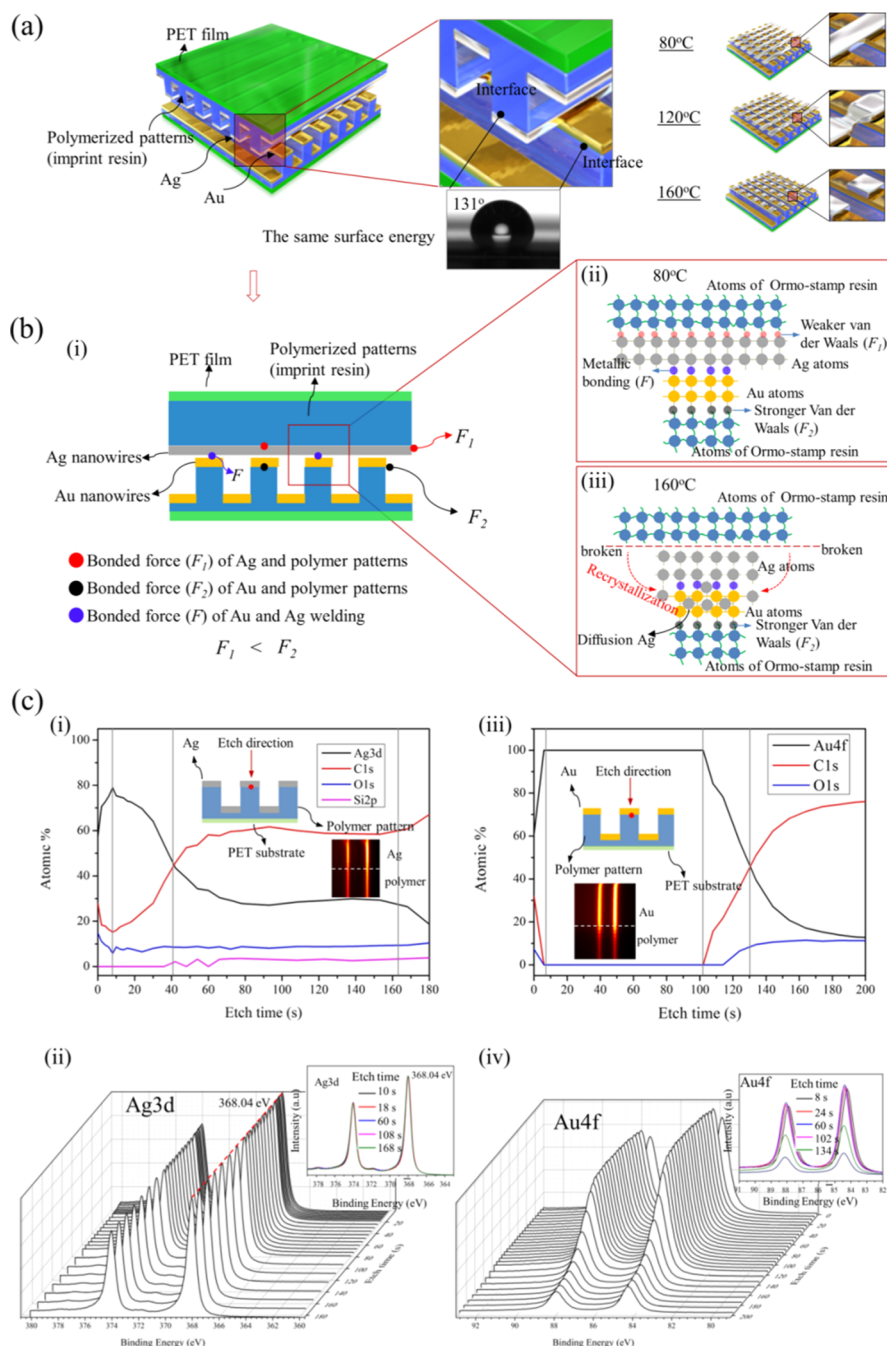


**Figure 3.** Mechanism of heterogeneous nanostructure formation by nanowelding. (a) Surface energies of polymer patterns. (b-i) Ag/polymer pattern interface has weak van der Waals forces ( $F_1$ ) because of the lower melting temperature of Ag, whereas Au/polymer pattern interface has strong van der Waals forces ( $F_2$ ). The metallic bonding force ( $F$ ) between Au and Ag is high because of nanowelding. Atomic structures at welding temperatures of (b-ii) 80 and (b-iii) 160 °C. (c) Binding energies of Ag/polymer and Au/polymer interfaces. (c-i) Variations in relative concentrations of nanostructures formed using Ag nanowires with etching time. (c-ii) Binding energies of Ag nanowires with different etching time. (c-iii) Variations in relative concentrations of different elements of nanostructures formed using Au nanowires with etching time. (c-iv) Corresponding binding energies with different etching time.

nanoimprinting, evaporation, and nanowelding. During the fabrication process, Ag nanowires transformed into nanoparticles with an increase in welding temperature, and the nanoparticles formed an ordered arrangement on the Au nanowire surfaces. The fabrication process is illustrated in Figure 1. The polymer pattern with dimensions of 100 nm × 200 nm × 150 nm on the PET substrate can be repeatedly replicated via nanoimprinting (see Figure 1a–d). Au and Ag nanowires were deposited on the fabricated polymer mold

using an e-beam evaporator (see Figure 1e,f). Then, nanowelding was performed via thermal nanoimprinting at 80 °C and 600 kPa for 10 min (see Figure 1g–i). Au and Ag nanowires were set into a cross pattern (see Figure 1g). After nanowelding, the Ag nanowires on the polymer pattern were transferred onto the Au nanowires because of the weaker bonding of the Ag/polymer interface than that of the Au/polymer interface. With an increase in welding temperature, the Ag nanowires undergo a dramatic change of shape until the

formation of Ag nanoparticles at a welding temperature of 160 °C (see Figure 1j–l).

Figure 2 shows the surface and cross-sectional morphologies of the fabricated samples and the mechanism of nanowelding. The dimensions of the Au and Ag nanowires were selected as 100 nm width, 200 nm pitch, and 30 nm thickness for the experiment. To determine the optimal welding temperature, various samples were fabricated using the proposed method under welding temperatures of 80–160 °C at intervals of 20 °C.

Figure 2a shows the morphologies and cross sections of the samples fabricated under different welding temperatures. In Figure 2a(i–v), we can observe that the shape of Ag nanowires changes with the increasing welding temperature from 80 to 160 °C at intervals of 20 °C. At the welding temperature of 80 °C, Au–Ag cross-composite nanowire arrays are successfully fabricated, as shown in Figure 2a(i,i-1). Figure 2a(ii,ii-1) shows cracks in the Ag nanowires welded at 100 °C. In addition, Ag nanorods are formed at a welding temperature of 120 °C (see Figure 2a(iii,iii-1)), whereas Ag nanoparticles are formed and arranged on the Au nanowire surfaces when welded at 160 °C (see Figure 2a(v,v-1)). From Figure 2a(i–v), we can conclude that the melting temperature of the Ag nanowire is lower than that of the Au nanowire.

Previous reports<sup>59–61</sup> have demonstrated that the melting temperature could vary depending on the size of metals at the nanoscale. Our group demonstrated Ag nanowires with size-dependent properties experimentally.<sup>62,63</sup> Here, we fabricated special nanostructures by exploiting different melting temperatures of Au and Ag. To verify the relative size effects of Ag and Au, Au and Ag nanowires with thicknesses of 30, 20, and 10 nm were fabricated via the proposed method. Figure 2b shows the morphologies and cross sections of the samples fabricated using Au and Ag nanowires with 10 and 30 nm thicknesses under different welding temperatures, respectively. We can observe that the 10 nm thick Au nanowires facilitated the transfer of 30 nm thick Ag nanowires via nanowelding because of the stronger bonding of Au with the polymer surface. In addition, both Au and Ag nanowires with thicknesses of 10, 20, and 30 nm were welded to better demonstrate the mutual influence based on different Au and Ag thicknesses. The morphologies and cross sections are shown in Supporting Information Figure S1.

**2.2. Mechanism of Formation of Heterogeneous Nanostructures.** To explain the phenomenon of transformation of nanowires into nanoparticles and the mechanism of transfer without surface treatment, a mechanism is proposed based on previous studies. Figure 3 displays the proposed mechanism of nanowelding and nanotransfer during the fabrication of nanostructures.

Au and Ag nanowires fabricated on the polymer patterns with the same surface energy were welded under an appropriate welding temperature (see Figure 3a). During nanowelding, the Ag nanowires were transferred onto the Au nanowire surfaces. With increasing welding temperatures, Ag nanowires begin to form nanorods and nanoparticles because of their increased melting temperatures (see Figure 3a). Only Ag nanowires were converted into nanoparticles at the welding temperature of 160 °C because Ag has a lower nanoscale melting temperature than that of Au. Figure 3b shows a schematic of the transfer process and the atoms of Au and Ag welded at 80 and 160 °C. The mutual bonding forces of Au, Ag, and the polymer pattern are illustrated in Figure 3b(i).  $F_1$ ,

$F_2$ , and  $F$  represent the bonding forces of Ag with the polymer pattern, Au with the polymer pattern, and Au with Ag, respectively. The experimental results shown in Figure 2 indicate that  $F_2$  is larger than  $F_1$ .

The bond between Ag nanowires and the polymer pattern breaks at a welding temperature of 80 °C because of the weaker van der Waals forces, as shown in Figure 3b(ii). Atoms of the contacting surfaces of the Ag and Au nanowires undergo metallic bonding ( $F$ ). Meanwhile, the van der Waals forces ( $F_2$ ) between Au nanowires and the polymer pattern are stronger than that between Ag nanowires and the polymer pattern ( $F_1$ ). Thus, the Ag nanowires are easily transferred onto the Au nanowires. With an increase in the welding temperature to 160 °C, the atoms of Ag nanowires become active and assemble into particles. In addition, some Ag atoms diffused into the Au nanowires, as shown in Figure 3b(iii). To verify the possibility of this transfer process without surface treatment and validate the mechanisms shown in Figure 3a,b, the binding energies of the interfaces of Ag, Au, and the polymer pattern were evaluated. In addition, the chemical compositions of the nanostructures were determined. Figure 3c shows the change in the binding energies of Au, Ag, and the polymer pattern. In this experiment, we chose an etching method to expose the interfaces of Au and Ag metals with the polymer pattern and thereby compare their binding energies. The measured method has been explained in detail in our previous works.<sup>56,62</sup> Figure 3c(i) shows the relative depth-dependent chemical compositions of the Ag nanowires on the polymer pattern with etching time. The etch image and cross-sectional schematic of the Ag nanowires on the polymer pattern are shown as insets in Figure 3c(i). The chemical elements Ag, C, and O are the most apparent, with their contents varying with etch time. After etching for 40 s, the percentage of C 1s continues to increase and gradually stabilizes. Thus, the Ag/polymer interface is exposed after an etch time of 40 s. To better compare the binding energies based on the etch time, the binding energy at each point of etching is shown in Figure 3c(ii). The same sharp peaks appear at each etch time. In addition, we chose several specific time points to observe the corresponding binding energies (see the inset in Figure 3c(ii)). The results indicate that the binding energy remains nearly constant. We can conclude that the van der Waals force between Ag nanowires and the polymer pattern is very small. Using the same method, the binding energy of the interface of Au nanowires and the polymer pattern was measured and evaluated. Figure 3c(iii) shows the relative chemical compositions of the Au nanowires on the polymer pattern with etching time. The etch image and cross-sectional schematic of the Au nanowires on the polymer pattern are shown as insets in Figure 3c(iii). The main chemical elements are Au, C, and O, and their contents vary with etching time. Beyond the etch time of 102 s, the Au content begins to decrease with continued etching, whereas the C and O contents increase. Therefore, the Au/polymer interface appears after an etch time of 102 s. In addition, the binding energy of each time point is shown in Figure 3c(iv), which indicates the shifting of binding energy at a critical etching time. This shift in the binding energy indicates that Au and polymer interactions occur at the interface. The existing studies<sup>64–66</sup> have reported and analyzed the binding energy shifts for metallic elements. Thus, Ag nanowires are easily transferred onto the Au nanowires by the nanowelding technology (see Figures 1 and 2). The binding energies of C

and O are shown in Supporting Information Figure S2 for reference.

**2.3. Recrystallization of Heterogeneous Nanostructures Composed of Two Metals.** Diffusion and recrystallization are shown in Figure 4. The mechanism shown in Figure 3 is consistent with the experimental results presented in Figure 2. However, to better observe and verify this proposed phenomenon, high-resolution TEM (HRTEM) images of the fabricated samples welded at 80, 100, and 160 °C were analyzed. To compare the cross-sectional changes in the samples fabricated at 120 and 140 °C, TEM and EDS mapping images are given in Figure S3. In addition, EDS mapping was performed to observe the distributions of Au and Ag. Figure 4 depicts the cross-sectional HRTEM and EDS mapping images of the fabricated samples.

The HRTEM images of Au–Ag composite nanowires with 30 nm thickness are shown in Figure 4a(i–v). Figure 4a(i) shows that the interface of Au nanowires (located in the bottom layer) with Ag nanowires (located at the top layer) is well-bonded at a welding temperature of 80 °C. The welding interface can be observed more clearly at a higher magnification (see Figure 4a(ii–iv)). In addition, the arrangement of Au and Ag atoms (see Figure 4a(v)) and the FFT image (shown in the inset) can be seen. As the welding temperature is increased, the Ag nanowires begin to break and become particulate in shape because of the decrease in melting temperature of Ag at the nanoscale. The transformation of Ag nanowires to particles is illustrated in Figure S3. Figure 4a(vi–ix) shows the EDS mapping images of the Au and Ag composite nanowires. Some Ag diffused into the Au nanowires (see Figure 4a(viii)) were induced by the lower melting temperature of Ag and the stronger attractive force of Au atoms under experimental conditions. Simultaneously, some Au were diffused into Ag (see Figure 4a(ix)). Figure 4b(i–v) shows the cross-sectional TEM images of the Au–Ag nanowires fabricated by welding at 100 °C. Figure 4c(i–v) shows the cross-sectional TEM images of the Au nanowire–Ag particle arrays fabricated by welding at 160 °C. Figure 4b(i) shows a cross-sectional TEM image of the heterogeneous nanostructure, with a 3D structure shown in the inset. Figure 4b(ii–iv) shows the HRTEM images of the welding interface. In the HRTEM images, Ag atoms are observed to diffuse into the Au nanowires depending on the melting temperature. To determine the composition and crystallization of Au and Ag, EDS mapping was performed, and the images are shown in Figure 4c(vi–ix). The results of Figure 4b,c are consistent with those of Figure 4a; only the welding temperature is different. The HRTEM and EDS mapping images elucidate the atomic arrangements and compositions of the heterostructures, respectively. To obtain crystallization and orientation information for the Ag–Au heterostructures, XRD analysis was performed, and the results are shown in Figure S4. The crystallization direction of Ag–Au is consistent with the findings of previous reports. Thus, the crystallization and direction of our fabricated Au nanowire–Ag nanoparticle arrays are proven.

**2.4. Transfer of Same-Species Metals without Surface Treatment.** To observe the fabrication process of the heterogeneous nanostructures, 3D images of the samples fabricated at welding temperatures of 80–160 °C were obtained by AFM. The AFM images of the fabricated samples are shown in Figure S5 for reference. In the described nanofabrication process, heterogeneous nanostructures were

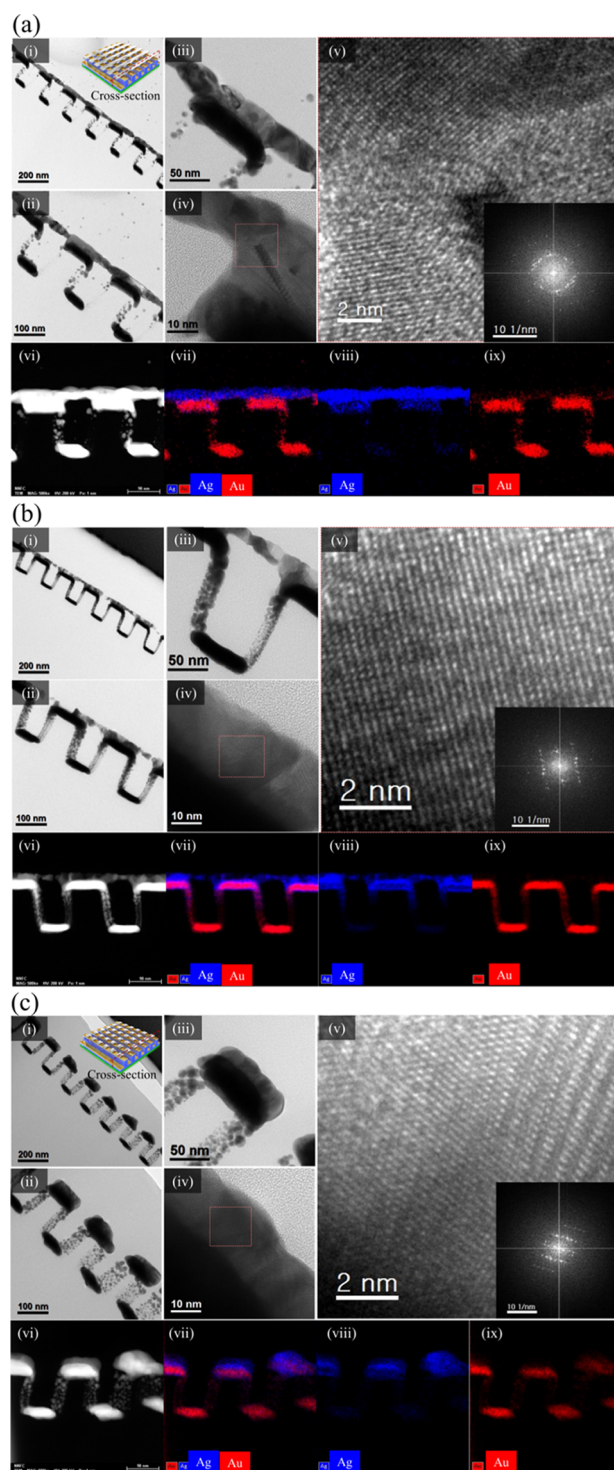


**Figure 4.** Cross-sectional TEM images and EDS mapping images of heterogeneous nanostructures fabricated at 80, 100, and 160 °C. (a) 80 °C; (i–v) TEM images of cross nanostructures at different magnifications [fast Fourier transform (FFT) image in the inset of v]; (vi–ix) EDS mapping images of cross nanostructures: (vi) composite, (vii) Ag and Au, (viii) Ag only, and (ix) Au only. (b) 100 °C; (i–v) TEM images at different magnifications (FFT image in the inset of v). (vi–ix) EDS mapping images of cross nanostructures: (vi) composite, (vii) Ag and Au, (viii) Ag only, and (ix) Au only. (c) 160 °C; (i–v) TEM images at different magnifications (FFT image in inset of v). (vi–ix) EDS mapping images of cross nanostructures: (vi) composite, (vii) Ag and Au, (viii) Ag only, and (ix) Au only.

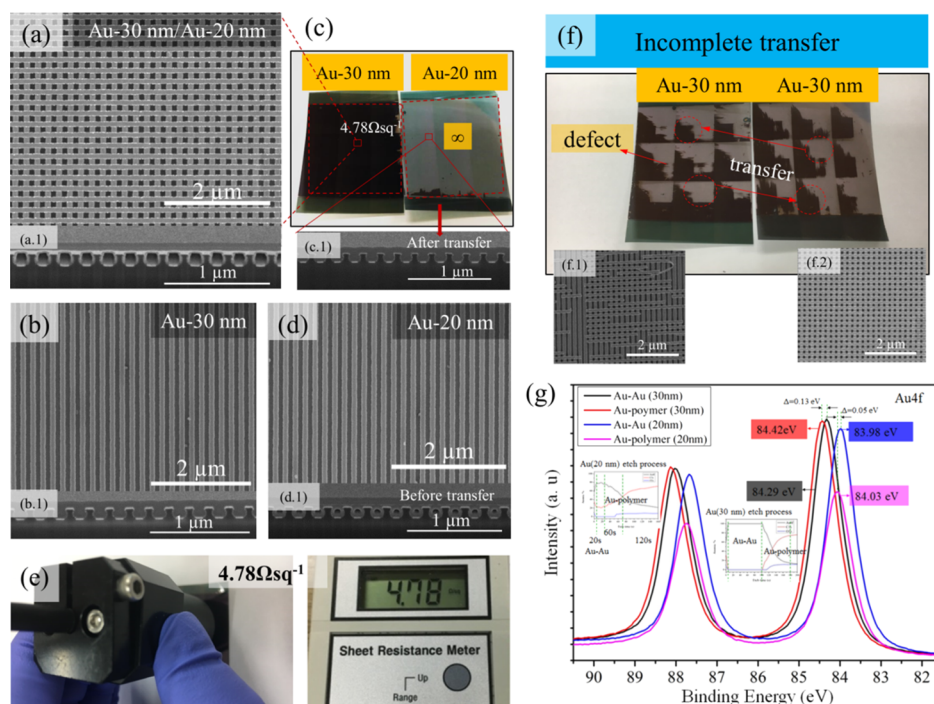


**Figure 5.** Transfer processes and mechanisms for same-metal components. (a) Morphology of cross nanostructure fabricated by nanowelding of 30 and 20 nm thick Au nanowires. (a.1) FIB cross-sectional image of the fabricated sample (lower layer is 30 nm; upper layer is 20 nm). (b) Morphology of 30 nm thick Au nanowires deposited on the polymer pattern. (b.1) FIB cross-sectional image. (c) Photographs after transfer of 30 and 20 nm thick Au nanowires. (c.1) FIB cross-sectional image after transfer. (d) Morphology of 20 nm thick Au nanowires deposited on the polymer pattern. (d.1) FIB cross-sectional image. (e) Measurement of sheet resistance of samples after transfer. (f) Photos and morphologies of 30 nm thick Au nanowires after transfer. (f.1) Morphology of incomplete transfer. (f.2) Morphology of a part with incomplete transfer. (g) Binding energies of Au–Au and Au–polymer for different nanowire thicknesses (etch process is shown in the inset).

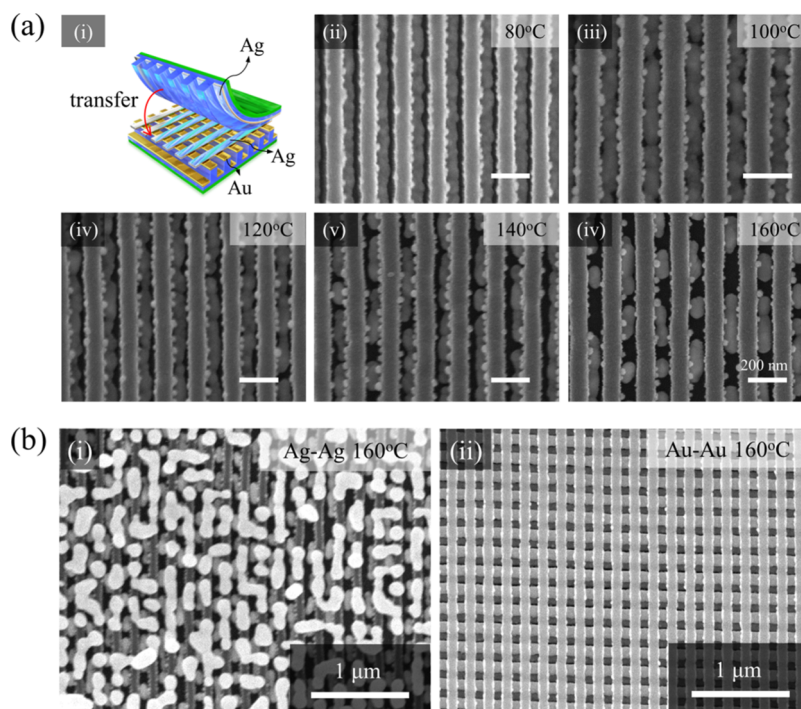


**Figure 6.** SEM images showing morphologies of well-ordered Ag nanowires and nanoparticles fabricated at different temperatures (80–160 °C in steps of 20 °C). (a) Morphologies of samples fabricated at temperatures of 80–160 °C; (i) schematic of transfer; SEM images of nanostructures fabricated at (ii) 80, (iii) 100, (iv) 120, (v) 140, and (vi) 160 °C. (b) Morphologies of Ag–Ag and Au–Au nanostructures fabricated at the welding temperature of 160 °C: (i) 20 nm Ag–Ag nanowire-based array; (ii) 20 nm Au–Au nanowire-based array.

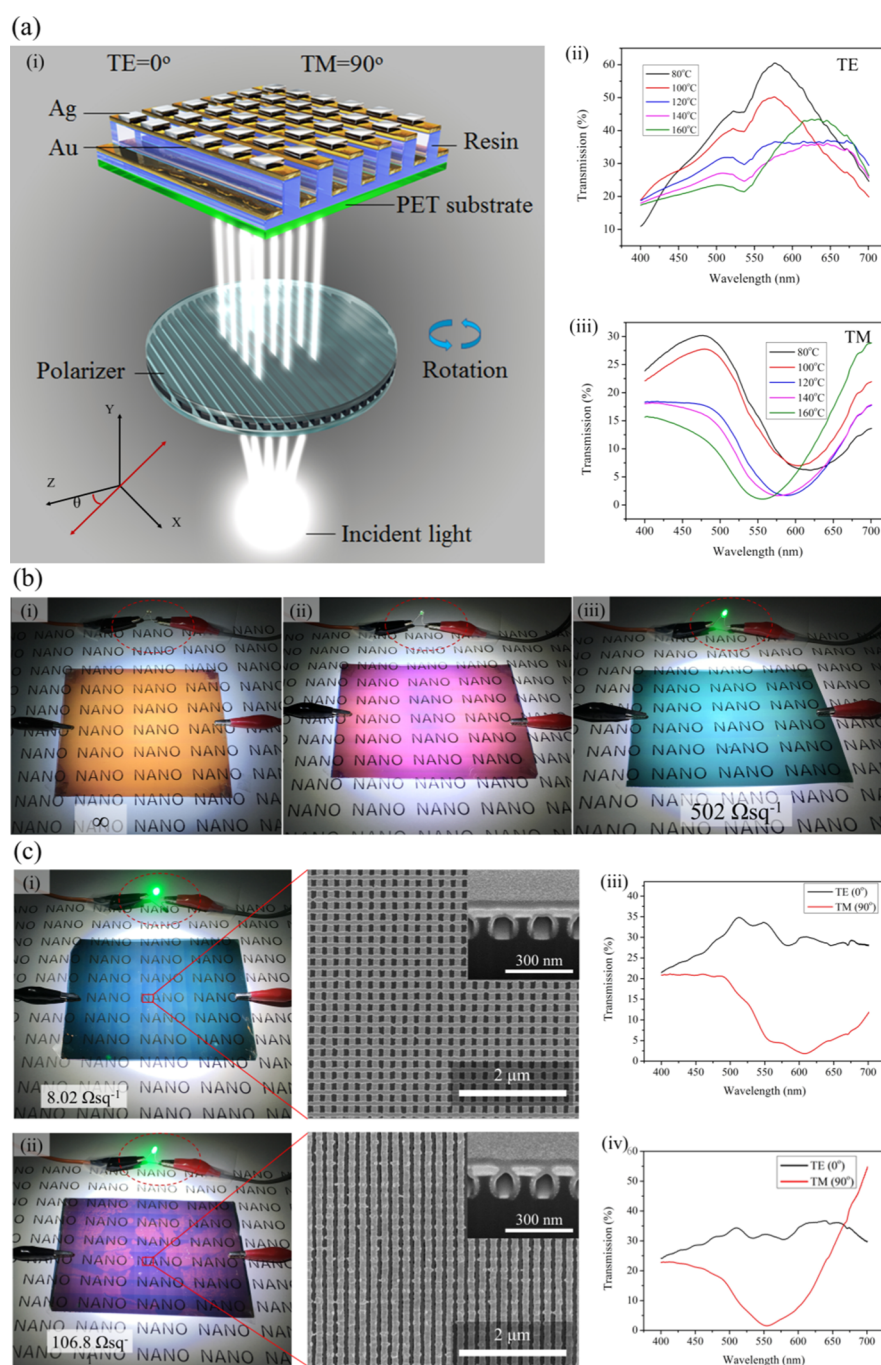


**Figure 7.** Transmission spectra and electronic properties of nanostructures fabricated at different temperatures. (a) Measurement of transmission spectra under TE and TM incident polarizations: (i) measurement schematic; (ii,iii) transmission spectra of nanostructures formed using Au and Ag nanowires with 30 nm thickness at 80–160 °C under TE and TM incident polarizations. (b) Electronic properties and transmission spectra of the samples comprising Ag and Au nanowires: color filter electrodes with (i) 10 nm Ag nanowires, (ii) 20 nm Ag nanowires, and (iii) 20 nm Au nanowires. (c) Electronic properties and transmission spectra of heterogeneous nanostructures fabricated using Ag and Au nanowires: color filter electrodes with (i) Ag and Au nanowires and (ii) Ag nanoparticles and Au nanowires; (iv–vi) corresponding polarization properties.

formed based on the different nanoscale melting temperatures of the two metals via nanowelding. During fabrication, no surface treatment was applied because of the interactions between Au and the polymer. To determine the feasibility of transfer of the same-species metal, Au nanowires with thicknesses of 30, 20, and 10 nm were used to investigate the same-metal nanowelding. Figure 5 presents the results of Au nanowire transfer via nanowelding.

The 20 nm thick Au nanowires easily transferred onto the 30 nm thick Au nanowires, as shown in Figure 5a. The morphologies and cross sections of the 30 nm thick Au nanowires are shown in Figure 5b,b.1, respectively. Photographs of the transferred samples with equal-sized nanowires are shown in Figure 5c. The 30 nm Au cross nanostructure is opaque with a sheet resistance of 4.78  $\Omega\text{sq}^{-1}$ , whereas the 20 nm Au cross nanostructure is transparent with a sheet resistance beyond the measurement range of our equipment.

The cross-sectional image of the post-transfer 20 nm sample is shown in Figure 5c(1). The morphology and cross-sectional image of the 20 nm thick Au nanowires are displayed in Figure 5d,d.1, respectively. The sheet resistance measurement is shown in Figure 5e. In addition, two 30 nm thick Au nanowires were nanowelded via the proposed method, and the results are shown in Figure 5f. The incompletely transferred sample is displayed in Figure 5f. The SEM images of a defect and partial transfer are depicted in Figure 5f.1,f.2, respectively. Transfer occurs incompletely because the polymer patterns have the same surface energies, whereas the metal/polymer interfaces have the same binding energies. In addition, previous studies have reported the size dependence of melting temperatures of noble metals at the nanoscale.<sup>67,68</sup> Thus, we can conclude that the melting temperature of 20 nm thick Au nanowires is lower than that of 30 nm thick Au nanowires. This may also facilitate the easy transfer of patterns. To confirm the underlying reason for a transfer, the binding energies of 30 and 20 nm thick Au nanowires were measured using the above-mentioned etching method that was used to obtain the results shown in Figure 3. Figure 5g shows the binding energies of Au nanowires with different thicknesses on the polymer patterns. The 30 and 20 nm thick Au nanowire etching profiles are shown in the inset in Figure 5g. The polymer/Au interfaces appear at different etch times. The specific etching process is given in Figure S6. The binding energies of specific etch points were also compared. Figure 5g shows that the Au–Au binding energy of the 30 nm thick nanowires is 84.29 eV, which is larger than that of the 20 nm thick nanowires (83.98 eV). The binding energy of the Au/polymer interface was evaluated with the increasing etching time. The shift in the binding energy of the 20 nm thick Au nanowires was very small compared to that of the 30 nm thick Au nanowires. This phenomenon explains the occurrence of a nanotransfer. To validate the mechanism of transfer of wires of different thicknesses, Au nanowires of 20 and 10 nm thicknesses were nanowelded, as shown in Figure S7, and the result shows that Au can be transferred well by adjusting the size without chemical treatment. To determine the transfer capability of other metals, Ag nanowires with 30, 20, and 10 nm thicknesses were evaluated using the same method, and the results are shown in Figure S8.

The proposed method can fabricate not only heterogeneous nanostructures but also arrays of Ag nanorods and nanoparticles with various welding temperatures. Figure 6a shows the SEM images of the transformation of Ag nanowires into particles with an increase in welding temperature. By this method, well-ordered Ag nanowires, nanorods, and nanoparticles are fabricated at different welding temperatures. Figure 6a(i) shows the schematic of the fabrication process. Well-ordered Ag nanowires are displayed in Figure 6a(ii). With an increase in the welding temperature, nanorods and nanoparticles were formed, as shown in Figure 6a(v,vi), respectively. Well-ordered nanostructures are located at the channel measuring 100 nm in width and 150 nm in depth. In future research, these well-ordered nanostructures will be separated from the channel to evaluate their properties.

To better compare the melting temperatures of Ag and Au, Ag–Ag nanowires and Au–Au nanowires were, respectively, nanowelded at 160 °C by the proposed method. Figure 6b shows the SEM images of the obtained Ag–Ag and Au–Au nanostructures. The Ag–Ag nanowires form nanoparticles at a high welding temperature of 160 °C, as shown in Figure 6b(i). In addition, high-quality Au–Au cross nanostructures are

displayed in Figure 6b(ii). Thus, the melting temperature of Au is higher than that of Ag at the nanoscale.

**2.5. Evaluation of Optical Properties and Color Filter Electrodes of Heterogeneous Nanostructures.** To evaluate the optical and electronic properties of the fabricated nanostructures, spectrometry and sheet resistance meter were used to measure their polarization properties and sheet resistance, respectively, as shown in Figure 7. The transmission spectra of the fabricated samples in response to transverse electric (TE) and transverse magnetic (TM) polarizations were measured, as shown schematically in Figure 7a(i). The fabricated nanostructures were placed on the polarizer, and the polarization properties were measured by rotating the polarizer. In this experiment, the polarization properties of the nanostructures comprising Au nanowires and Ag nanowires of different thicknesses were measured according to the welding temperature.

Figure 7a(ii,iii) shows the welding temperature-dependent transmission spectra of 30 nm Au/30 nm Ag nanostructures fabricated at 80–160 °C at intervals of 20 °C in response to TE and TM incident polarizations. Here, we define TE and TM coordinates based on Au nanostructure, to which TE axis is parallel. Then, as shown in Figure 7a(ii), TE mode for Au nanostructures could be considered as TM mode for Ag nanostructures because of the orthogonal relationship of Ag and Au nanostructures. During incident light irradiation of the nanostructures through a polarizer, if the frequency of the photons in the incident light is the same as that of the electrons at the metal surface, photonic and electronic resonances occur, which are called surface plasmon resonances (SPRs). The peak originating from this phenomenon appears at a special wavelength. As the welding temperature increases, the shape of the fabricated nanostructures begins to change. Therefore, resonance occurs at a different wavelength. Under TE mode, the transmission decreases with the increasing welding temperature. In addition, the resonant peak is red-shifted. However, under TM incident polarization, a blue shift is observed with the increasing welding temperature. The welding temperature-dependent transmission spectra of the nanostructures comprising 20 nm Au/30 nm Ag fabricated at 80–160 °C at intervals of 20 °C in response to TE and TM incident polarizations are shown in Figure S9. In general, the resonance peak in a nanostructure could be enhanced in two manners—sharpness and overall enhancement in transmittance. In a proposed nanostructure, we could control the resonance peak in the TE mode by thickness of Ag grating. However, grating thickness control usually influences both sharpness and the overall enhancement of the resonance peak in an inverse manner. The effective way to improve both of the two characteristics of the resonance peak controls the grating design parameters—period and duty cycle—in addition to changing grating thickness. It could be the next research about the extent of design possibility with the above-mentioned scheme. Under the TE mode, the transmission decreases with the increasing welding temperature, and the resonant peak is red-shifted, whereas under TM incident polarization, a blue shift is observed with the increasing welding temperature. As observed, the change in the optical properties of the fabricated samples based on different welding temperatures can be utilized in various devices such as biosensors, gas sensors, and plasmonic color filters. To demonstrate the feasibility of a large-area flexible fabrication,

a sample with dimensions of 120 mm × 120 mm is shown in Figure S10.

Recently, color filter electrodes<sup>69,70</sup> have become noticeable because of their enormous potential for applications in optical devices, including large-area devices and flexible devices. To explore a potential application, color filter electrodes with polarization properties were fabricated via the proposed method. The sheet resistance and polarization properties of the color filters were measured and evaluated. Figure 7b shows the sheet resistance and color images of the fabricated samples. Various colors can be obtained by changing the thickness, materials, and shapes of the nanostructures. A color filter electrode with 10 nm thick Ag nanowires is shown in Figure 7b(i). The electrode is yellow because of the appearance of special resonance. The corresponding polarization properties are shown in Figure S11a. Because of the low thickness of the Ag nanowires, the sheet resistance is very high. In this experiment, we also used a light-emitting diode (LED) to evaluate the conductivity of the fabricated color filters. Figure 7b(ii) shows a color filter electrode fabricated using 20 nm thick Ag nanowires; the electrode is purple and the brightness of the LED can be observed. Its corresponding polarization properties are shown in Figure S11b. A color filter electrode fabricated using 20 nm thick Au nanowires is shown in Figure 7b(iii); the electrode is green and the corresponding polarization properties are displayed in Figure S11c. The brightness of the LED is stronger than that of the electrode shown in Figure 7b(ii) because of the smaller sheet resistance. To improve the conductivity of the above-mentioned samples, the sheet resistance and transmission spectra of the fabricated heterogeneous nanostructures were evaluated via the proposed method. Figure 7c shows the sheet resistance and transmission spectra of the heterogeneous nanostructures fabricated using Au and Ag nanowires with thicknesses of 20 nm. Figure 7c(i) shows a color filter with a sheet resistance of  $8.02 \Omega \text{ sq}^{-1}$  as well as its morphology and cross-sectional image (inset); the corresponding polarization properties are displayed in Figure 7c(iii). When the polarizer is rotated, incident light cannot pass through the nanostructure at special wavelengths for the TM mode because of rectangular nanostructure and vice versa. Figure 7c(ii) shows a color filter with a sheet resistance of  $106.8 \Omega \text{ sq}^{-1}$  as well as its morphology and cross-sectional image (inset); the corresponding polarization properties are displayed in Figure 7c(iv). As we know, transmittance curves caused by the SPR phenomenon depend on structures and materials. In this work, we fabricated 2D structural symmetric array, but with different materials at each axis, so this nanostructure should have polarization dependence characteristics because of optical heterogeneity in the array axis. This effect would result in our drastic difference in TE and TM spectra. Plus, this point also indicates that we presented drastic polarization dependence with only one grating design by our nanowelding technique with different materials. The proposed heterogeneous nanostructures have significant potential applicability, especially in flexible devices and large-area devices.

### 3. CONCLUSIONS

In summary, a novel method for fabricating heterogeneous nanostructures was proposed based on nanowelding at various temperatures. Ag nanoparticles with an orderly arrangement were fabricated on the surface of Au nanowires. The morphologies and cross sections of the samples fabricated in

the welding temperature range of 80–160 °C were observed. Various heterogeneous nanostructures were obtained at different welding temperatures because of the difference in the melting temperatures of the nanoscale noble metals. The mechanism of the nanostructure transfer was demonstrated via measurements and experiments. On the basis of the proposed transfer mechanism, which relies on the different binding energies between the metals and the polymer pattern, the transfer of single-species metal components via nanowelding without chemical treatment was experimentally demonstrated and discussed. The experiments showed that the transfer of single-species metal components was easily achieved through nanowelding without chemical treatment. The optical properties of the fabricated samples were evaluated by spectrometry and showed a welding temperature dependence. In addition, color filter electrodes with polarization properties were fabricated and evaluated, demonstrating a potential application. We believe that our proposed method may have a significant impact on the fields of display devices, biosensors, and plasmonic devices.

## 4. EXPERIMENTAL SECTION

**4.1. Fabrication of Heterogeneous Nanostructures.** The proposed heterogeneous nanostructures were fabricated based on different melting temperatures of two different metals. The fabrication process of Figure 1a–f has been explained in our previous works.<sup>56,62</sup> The deposited Au and Ag nanowires were set into the designed shape, and nanowelding was performed at 80 °C and 600 kPa for 10 min (see Figure 1g). After nanowelding, a detachment process was implemented (see Figure 1h,i). The Ag nanowires were transferred onto the Au nanowire surfaces by recrystallization of Ag and Au atoms. During the transfer process, the Ag nanowires were successfully transferred onto the Au nanowires under the same surface energy as that of the polymer pattern. This is because the binding energy of Au with the polymer was stronger than that of the polymer with Ag, as discussed in section 3. As the welding temperature was increased, the Ag nanowires gradually melted into particles (see Figure 7j–l). The Ag nanoparticles formed a local ordered arrangement on the Au nanowires because of the bonding forces among the atoms, as discussed in section 3.

**4.2. Characterization.** The morphologies and cross sections were analyzed by field-emission SEM (FE-SEM; Sirion, FEI, Netherlands) and FIB (Helios, FEI, Netherlands) imaging, respectively. To clearly observe the 3D images of the transition from Ag nanowires to particles based on the variation in welding temperatures, AFM (XE-100, Park Systems) was performed. Further, TEM (JEM-ARM200F, JEOL, Japan) was performed to analyze the changes in Ag and Au atoms, whereas EDS mapping was performed to observe the elemental distributions of Ag and Au. In addition, XRD (MXD10, SmartLab, Rigaku Corporation, Japan) was conducted to analyze the crystal orientation and crystallization, whereas XPS (K-Alpha+, Thermo Fisher Scientific, Inc.) was performed to determine the compositions and measure the binding energies at the interfaces of Ag, Au, and polymer pattern. An optical microscope (Eclipse LV 100, Nikon Instruments, Inc., USA) and a spectrometer (QE Pro 6000, Ocean Optics, USA) were used to evaluate the optical properties of the fabricated samples.

## ■ ASSOCIATED CONTENT

### Supporting Information

The Supporting Information is available free of charge on the ACS Publications website at DOI: 10.1021/acsami.8b18405.

Characterizations of welded structures of 30, 20 nm, and 10 nm thick Au nanowires with 20 nm thick Ag nanowires at different temperatures; transfer processing of same-metal welded structures; welding temperature-

dependent transmission spectra of Au–Ag nanostructures; and large-area flexible fabrication of same-metal and different-metal nanostructure arrays(PDF)

## AUTHOR INFORMATION

### Corresponding Author

\*E-mail: [jhjeong@kimm.re.kr](mailto:jhjeong@kimm.re.kr).

### ORCID

Inkyu Park: 0000-0001-5761-7739

Jun-Ho Jeong: 0000-0003-0671-0225

### Funding

This work was supported by the Center for Advanced Meta-Materials (CAMM) funded by the Ministry of Science, ICT and Future Planning, Korea, through the Global Frontier Project (CAMM-no. 2014M3A6B3063707) and by the Industrial Strategic Technology Development Program (10052641) funded by Ministry of Trade, Industry & Energy (MI, Korea).

### Notes

The authors declare no competing financial interest.

## REFERENCES

- (1) Hartland, G. V. Optical Studies of Dynamics in Noble Metal Nanostructures. *Chem. Rev.* **2011**, *111*, 3858–3887.
- (2) Sheldon, M. T.; van de Groep, J.; Brown, A. M.; Polman, A.; Atwater, H. A. Plasmoelectric Potentials in Metal Nanostructures. *Science* **2014**, *346*, 828–831.
- (3) Zhang, R.; Bursi, L.; Cox, J. D.; Cui, Y.; Krauter, C. M.; Alabastri, A.; Manjavacas, A.; Calzolari, A.; Corni, S.; Molinari, E.; Carter, E. A.; García de Abajo, F. J.; Zhang, H.; Nordlander, P. How to Identify Plasmons from the Optical Response of Nanostructures. *ACS Nano* **2017**, *11*, 7321–7335.
- (4) Seeman, N. C.; Belcher, A. M. Emulating Biology: Building Nanostructures from the Bottom Up. *Proc. Natl. Acad. Sci. U.S.A.* **2002**, *99*, 6451–6455.
- (5) Weerasekera, H. D. A.; Silvero, M. J.; Regis Correa da Silva, D.; Scaiano, J. C.; Scaiano, J. C. A Database on the Stability of Silver and Gold Nanostructures for Applications in Biology and Biomolecular Sciences. *Biomater. Sci.* **2017**, *5*, 89–97.
- (6) Rytka, C.; Kristiansen, P. M.; Neyer, A. Isoand Variothermal Injection Compression Moulding of Polymer Micro- and Nanostructures for Optical and Medical Applications. *J. Micromech. Microeng.* **2015**, *25*, 065008.
- (7) Matsuura, N.; Rowlands, J. A. Towards New Functional Nanostructures for Medical Imaging. *Med. Phys.* **2008**, *35*, 4474–4487.
- (8) Narasimhan, V.; Siddique, R. H.; Lee, J. O.; Kumar, S.; Ndjamen, B.; Du, J.; Hong, N.; Sretavan, D.; Choo, H. Multifunctional Biophotonic Nanostructures Inspired by the Longtail Glasswing Butterfly for Medical Devices. *Nat. Nanotechnol.* **2018**, *13*, 512–519.
- (9) Balasubramanian, K.; Tirumali, M.; Badhe, Y.; Mahajan, Y. R. Nano-enabled Multifunctional Materials for Aerospace Applications. In *Aerospace Materials and Material Technologies*; Prasad, N. E., Wanhill, R. J. H., Eds.; Springer: Singapore, 2017; Chapter 19, pp. 439–453.
- (10) Diegoli, S.; Hamlett, C. A. E.; Leigh, S. J.; Mendes, P. M.; Preece, J. A. Engineering Nanostructures at Surfaces Using Nanolithography. *Proc. Inst. Mech. Eng., Part G* **2007**, *221*, 589–629.
- (11) Dontha, N.; Nowall, W. B.; Kuhr, W. G. Generation of Biotin/Avidin/Enzyme Nanostructures with Maskless Photolithography. *Anal. Chem.* **1997**, *69*, 2619–2625.
- (12) Rühle, J. And There Was Light: Prospects for the Creation of Micro- and Nanostructures through Maskless Photolithography. *ACS Nano* **2017**, *11*, 8537–8541.
- (13) Donthu, S.; Pan, Z.; Myers, B.; Shekhawat, G.; Wu, N.; Dravid, V. Facile Scheme for Fabricating Solid-State Nanostructures Using E-Beam Lithography and Solution Precursors. *Nano Lett.* **2005**, *5*, 1710–1715.
- (14) Chen, Y. Nanofabrication by Electron Beam Lithography and Its Applications: A Review. *Microelectron. Eng.* **2015**, *135*, 57–72.
- (15) Drost, M.; Tu, F.; Berger, L.; Preischl, C.; Zhou, W.; Gliemann, H.; Wöll, C.; Marbach, H. Surface-Anchored Metal-Organic Frameworks as Versatile Resists for Gas-Assisted E-Beam Lithography: Fabrication of Sub-10 Nanometer Structures. *ACS Nano* **2018**, *12*, 3825–3835.
- (16) Steglich, M.; Käsebier, T.; Zilk, M.; Pertsch, T.; Kley, E.-B.; Tünnermann, A. The Structural and Optical Properties of Black Silicon by Inductively Coupled Plasma Reactive Ion Etching. *J. Appl. Phys.* **2014**, *116*, 173503.
- (17) Wu, J.; Ye, X.; Sun, L.; Huang, J.; Wen, J.; Geng, F.; Zeng, Y.; Li, Q.; Yi, Z.; Jiang, X.; Zhang, K. Growth Mechanism of One-step Self-Masking Reactive-Ion-Etching (RIE) Broadband Antireflective and Superhydrophilic Structures Induced by Metal Nanodots on Fused Silica. *Opt. Express* **2018**, *26*, 1361–1374.
- (18) Kanda, T.; Fukusato, T.; Matsuda, M.; Toyoda, K.; Oba, H.; Kotoku, J.; Haruyama, T.; Kitajima, K.; Furui, S. Gadolinium-based Contrast Agent Accumulates in the Brain Even in Subjects without Severe Renal Dysfunction: Evaluation of Autopsy Brain Specimens with Inductively Coupled Plasma Mass Spectroscopy. *Radiology* **2015**, *276*, 228–232.
- (19) Qu, H.; Linder, S. W.; Mudalige, T. K. Surface Coating and Matrix Effect on the Electrophoretic Mobility of Gold Nanoparticles: A Capillary Electrophoresis-Inductively Coupled Plasma Mass Spectrometry Study. *Anal. Bioanal. Chem.* **2016**, *409*, 979–988.
- (20) Chou, S. Y.; Krauss, P. R.; Renstrom, P. J. Nanoimprint Lithography. *J. Vac. Sci. Technol., B: Microelectron. Nanometer Struct.–Process., Meas., Phenom.* **1996**, *14*, 4129.
- (21) Park, S. J.; Ok, J. G.; Park, H. J.; Lee, K.-T.; Lee, J. H.; Kim, J. D.; Cho, E.; Baac, H. W.; Kang, S.; Guo, L. J.; Hart, A. J. Modulation of the Effective Density and Refractive Index of Carbon Nanotube Forests via Nanoimprint Lithography. *Carbon* **2018**, *129*, 8–14.
- (22) Seshan, K.; Schepis, D. *Handbook of Thin Film Deposition*; Elsevier: Norwich, NY, USA, 2018.
- (23) Chrisey, D. B.; Hubler, G. K. *Pulsed Laser Deposition of Thin Films*; Wiley: Hoboken, NJ, USA, 1994.
- (24) Yoon, S.-S.; Khang, D.-Y. Facile Patterning of Ag Nanowires Network by Micro-Contact Printing of Siloxane. *ACS Appl. Mater. Interfaces* **2016**, *8*, 23236–23243.
- (25) Fodor, S.; Read, J.; Pirrung, M.; Stryer, L.; Lu, A.; Solas, D. Light-Directed, Spatially Addressable Parallel Chemical Synthesis. *Science* **1991**, *251*, 767–773.
- (26) Sancheti, S. V.; Gogate, P. R. A Review of Engineering Aspects of Intensification of Chemical Synthesis Using Ultrasound. *Ultrason. Sonochem.* **2017**, *36*, 527–543.
- (27) Kristensen, A.; Yang, J. K. W.; Bozhevolnyi, S. I.; Link, S.; Nordlander, P.; Halas, N. J.; Mortensen, N. A. Plasmonic colour generation. *Nat. Rev. Mater.* **2017**, *2*, 16088.
- (28) Kim, D. G.; Kim, S. H.; Ki, H. C.; Kim, T. U.; Kim, H.-S.; Choi, Y. W.; Jo, M. H.; Shin, J. C. Optical Characteristics of Double Layered Plasmonic Structure Using Nanopatterning Process. *J. Nanosci. Nanotechnol.* **2018**, *18*, 1913–1916.
- (29) Ogawa, S.; Kimata, M. Direct Fabrication and Characterization of High-Aspect-Ratio Plasmonic Nanogratings Using Tapered-Side-wall Molds. *Opt. Mater. Express* **2017**, *7*, 633–640.
- (30) Liu, C.; Meng, F.; Wang, B.; Zhang, L.; Cui, X. Plasmonic Nanograting Enhanced Fluorescence for Protein Microarray Analysis of Carcinoembryonic Antigen (CEA). *Anal. Methods* **2018**, *10*, 145–150.
- (31) Pfeiffer, M.; Atkinson, P.; Rastelli, A.; Schmidt, O. G.; Giessen, H.; Lippitz, M.; Lindfors, K. Coupling a Single Solid-State Quantum Emitter to an Array of Resonant Plasmonic Antennas. *Sci. Rep.* **2018**, *8*, 3415.
- (32) Matsuzaki, K.; Vassant, S.; Liu, H.-W.; Dutschke, A.; Hoffmann, B.; Chen, X.; Christiansen, S.; Buck, M. R.; Hollingsworth, J. A.; Götzinger, S.; Sandoghdar, V. Strong Plasmonic Enhancement of

Biexciton Emission: Controlled Coupling of a Single Quantum Dot to a Gold Nanocone Antenna. *Sci. Rep.* **2017**, *7*, 42307.

(33) Yun, H.; Lee, S.-Y.; Hong, K.; Yeom, J.; Lee, B. Plasmonic Cavity-Apertures as Dynamic Pixels for the Simultaneous Control of Colour and Intensity. *Nat. Commun.* **2015**, *6*, 7133.

(34) Pedross-Engel, A.; Arnitz, D.; Gollub, J. N.; Yurduseven, O.; Trofatter, K. P.; Imani, M. F.; Sleasman, T.; Boyarsky, M.; Fu, X.; Marks, D. L.; Smith, D. R.; Reynolds, M. S. Orthogonal Coded Active Illumination for Millimeter Wave, Massive-MIMO Computational Imaging With Metasurface Antennas. *Opt. Mater. Express* **2018**, *4*, 184–193.

(35) Sun, Z.; Zhou, S.; Gu, Y.; Zhao, Y. A Quaternary Ammonium Modified Coumarin Derivative for Antimicrobial Photodynamic Therapy. *Proceedings of SPIE 10497, Light-Based Diagnosis and Treatment of Infectious Diseases*; International Society for Optics and Photonics: Bellingham, WA, USA, 2018; p 104790Z.

(36) Sun, M.; Xu, L.; Ma, W.; Wu, X.; Kuang, H.; Wang, L.; Xu, C. Hierarchical Plasmonic Nanorods and Upconversion Core-Satellite Nanoassemblies for Multimodal Imaging-Guided Combination Phototherapy. *Adv. Mater.* **2015**, *28*, 898–904.

(37) Wilson, W. M.; Stewart, J. W.; Mikkelsen, M. H. Surpassing Single Line Width Active Tuning with Photochromic Molecules Coupled to Plasmonic Nanoantennas. *Nano Lett.* **2018**, *18*, 853–858.

(38) Wang, Z.; Guo, Z. Biomimetic Superwetable Materials with Structural Colours. *Chem. Commun.* **2017**, *53*, 12990–13011.

(39) Wang, Z.; Guo, Z. Biomimetic Photonic Structures with Tunable Structural Colours: From Natural to Biomimetic to Applications. *J. Bionic Eng.* **2018**, *15*, 1–33.

(40) Moeck, P.; DeStefano, P. Accurate Lattice Parameters from 2D-Periodic Images for Subsequent Bravais Lattice Type Assignments. *Adv. Struct. Chem. Imaging* **2018**, *4*, 5.

(41) Jia, X.; Bowen, P.; Huang, Z.; Liu, X.; Bingham, C.; Smith, D. R. Clarification of Surface Modes of a Periodic Nanopatch Metasurface. *Opt. Express* **2018**, *26*, 3004–3012.

(42) Shin, W.; Cho, W.; Baik, S. J. Silver Nanowires Network Encapsulated by Low Temperature Sol–Gel ZnO for Transparent Flexible Electrodes with Ambient Stability. *Mater. Res. Express* **2018**, *5*, 015050.

(43) Fang, Y.; Wu, Z.; Li, J.; Jiang, F.; Zhang, K.; Zhang, Y.; Zhou, Y.; Zhou, J.; Hu, B. High-Performance Hazy Silver Nanowire Transparent Electrodes through Diameter Tailoring for Semi-transparent Photovoltaics. *Adv. Funct. Mater.* **2018**, *28*, 1705409.

(44) Zhang, Y.; Guo, J.; Xu, D.; Sun, Y.; Yan, F. One-Pot Synthesis and Purification of Ultralong Silver Nanowires for Flexible Transparent Conductive Electrodes. *ACS Appl. Mater. Interfaces* **2017**, *9*, 25465–25473.

(45) Kang, M. S.; Joh, H.; Kim, H.; Yun, H.-W.; Kim, D.; Woo, H. K.; Lee, W. S.; Hong, S.-H.; Oh, S. J. Synergetic Effects of Ligand Exchange and Reduction Process Enhancing Both Electrical and Optical Properties of Ag Nanocrystals for Multifunctional Transparent Electrodes. *Nanoscale* **2018**, *10*, 18415–18422.

(46) Yang, J.; Bao, C.; Zhu, K.; Yu, T.; Xu, Q. High-Performance Transparent Conducting Metal Network Electrodes for Perovskite Photodetectors. *ACS Appl. Mater. Interfaces* **2018**, *10*, 1996–2003.

(47) Oh, H.; Lee, S.-W.; Kim, M.; Lee, W. S.; Seong, M.; Joh, H.; Allen, M. G.; May, G. S.; Bakir, M. S.; Oh, S. J. Designing Surface Chemistry of Silver Nanocrystals for Radio Frequency Circuit Applications. *ACS Appl. Mater. Interfaces* **2018**, *10*, 37643–37650.

(48) Liang, J.; Zhu, K.; Yang, R.; Hu, M. Room temperature NO<sub>2</sub> sensing properties of Au-decorated vanadium oxide nanowires sensor. *Ceram. Int.* **2018**, *44*, 2261–2268.

(49) Saravanan, R.; Mansoob Khan, M.; Gupta, V. K.; Mosquera, E.; Gracia, F.; Narayanan, V.; Stephen, A. ZnO/Ag/CdO Nanocomposite for Visible Light-Induced Photocatalytic Degradation of Industrial Textile Effluents. *J. Colloid Interface Sci.* **2015**, *452*, 126–133.

(50) Long, G.; Sabalo, K.; MacDonald, N.; Beattie, M.; Sadoqi, M. Photocurrent Enhancement by Introducing Gold Nanoparticles in Nanostructures Based Heterojunction Solar Cell Device. *MRS Adv.* **2017**, *2*, 817–824.

(51) Li, C.; Jiang, F.; Liu, C.; Wang, W.; Li, X.; Wang, T.; Xu, J. A Simple Thermoelectric Device Based on Inorganic/Organic Composite Thin Film for Energy Harvesting. *Chem. Eng. J.* **2017**, *320*, 201–210.

(52) Yin, Z.; Wang, Y.; Song, C.; Zheng, L.; Ma, N.; Liu, X.; Li, S.; Lin, L.; Li, M.; Xu, Y.; Li, G.; Hu, G.; Fang, Z.; Ma, D. Hybrid Au-Ag Nanostructures for Enhanced Plasmon-Driven Catalytic Selective Hydrogenation through Visible Light Irradiation and Surface-Enhanced Raman Scattering. *J. Am. Chem. Soc.* **2018**, *140*, 864–867.

(53) Hwang, C. S.; Lee, Y.; Ahn, M.; Chung, T.; Jeong, K. Visible range subtractive plasmonic color filter arrays using Ag-Au alloyed nanoislands. *Micro Electro Mechanical Systems (MEMS), 2018 IEEE*, 2018; pp 535–538.

(54) Han, Q.; Zhang, C.; Gao, W.; Han, Z.; Liu, T.; Li, C.; Wang, Z.; He, E.; Zheng, H. Ag-Au alloy nanoparticles: Synthesis and in situ monitoring SERS of plasmonic catalysis. *Sens. Actuators, B* **2016**, *231*, 609–614.

(55) Hwang, B.; Shin, S.-H.; Hwang, S.-H.; Jung, J.-Y.; Choi, J.-H.; Ju, B.-K.; Jeong, J.-H. Flexible Plasmonic Color Filters Fabricated via Nanotransfer Printing with Nanoimprint-Based Planarization. *ACS Appl. Mater. Interfaces* **2017**, *9*, 27351–27356.

(56) Zhao, Z.-J.; Hwang, S. H.; Jeon, S.; Hwang, B.; Jung, J.-Y.; Lee, J.; Park, S.-H.; Jeong, J.-H. Three-Dimensional Plasmonic Ag/TiO<sub>2</sub> Nanocomposite Architectures on Flexible Substrates for Visible-Light Photocatalytic Activity. *Sci. Rep.* **2017**, *7*, 8915.

(57) Toki, M.; Honda, M. Strengthened Glass Substrates for Polarizers and Color Filters. U.S. Patent 20,160,216,558 A1, 2016.

(58) Zhao, Z.-J.; Lee, M.; Kang, H.; Hwang, S.; Jeon, S.; Park, N.; Park, S.-H.; Jeong, J.-H. Eight Inch Wafer-Scale Flexible Polarization-Dependent Color Filters with Ag-TiO<sub>2</sub> Composite Nanowires. *ACS Appl. Mater. Interfaces* **2018**, *10*, 9188–9196.

(59) Buffat, P.; Borel, J.-P. Size Effect on the Melting Temperature of Gold Particles. *Phys. Rev. A: At., Mol., Opt. Phys.* **1976**, *13*, 2287.

(60) Li, T. X.; Ji, Y. L.; Yu, S. W.; Wang, G. H. Melting Properties of Noble Metal Clusters. *Solid State Commun.* **2000**, *116*, 547–550.

(61) Castro, T.; Reifengerger, R.; Choi, E.; Andres, R. P. Size-Dependent Melting Temperature of Individual Nanometer-Sized Metallic Clusters. *Phys. Rev. B: Condens. Matter Mater. Phys.* **1990**, *42*, 8548.

(62) Zhao, Z.-J.; Shin, S.-H.; Choi, D.-G.; Park, S.-H.; Jeong, J.-H. Shape-Controlled 3D Periodic Metal Nanostructures Fabricated via Nanowelding. *Small* **2017**, *14*, 1870023.

(63) Zhao, Z.-J.; Hwang, S. H.; Jeon, S.; Jung, J.-Y.; Lee, J.; Choi, D.-G.; Choi, J.-H.; Park, S.-H.; Jeong, J.-H. Effects of Polymer Surface Energy on Morphology and Properties of Silver Nanowire Fabricated via Nanoimprint and E-beam Evaporation. *Appl. Surf. Sci.* **2017**, *420*, 429–438.

(64) Citrin, P. H.; Wertheim, G. K.; Baer, Y. Core-level binding energy and density of states from the surface atoms of gold. *Phys. Rev. Lett.* **1978**, *41*, 1425.

(65) Johansson, B.; Mårtensson, N. Core-level binding-energy shifts for the metallic elements. *Phys. Rev. B: Condens. Matter Mater. Phys.* **1980**, *21*, 4427.

(66) Williams, A. R.; Lang, N. D. Core-level binding-energy shifts in metals. *Phys. Rev. Lett.* **1978**, *40*, 954.

(67) Jiang, Q.; Zhang, S.; Zhao, M. Size-Dependent Melting Point of Noble Metals. *Mater. Chem. Phys.* **2003**, *82*, 225–227.

(68) Hasegawa, M.; Watabe, M.; Hoshino, K. A Theory of Melting in Metallic Small Particles. *J. Phys. F: Metal Phys.* **1980**, *10*, 619–635.

(69) Choi, K. C.; Han, J. H. Organic Light Emitting Diode Device Integrated with Color Filter Electrode and Method of Manufacturing the Same. U.S. Patent 20,180,108,709 A1, 2018.

(70) Han, J. H.; Kim, D.-Y.; Kim, D.; Choi, K. C. Highly Conductive and Flexible Color Filter Electrode Using Multilayer Film Structure. *Sci. Rep.* **2016**, *6*, 29341.